\$ SUPER

Contents lists available at ScienceDirect

Nano Energy

journal homepage: www.elsevier.com/locate/nanoen





Ductile (Ag,Cu)₂(S,Se,Te)-based auxetic metamaterials for sustainable thermoelectric power generation

Seong Eun Yang ^{a,1}, Youngtaek Oh ^{b,1}, Jungsoo Lee ^a, Seungheon Shin ^b, So-Hyeon Lee ^c, Keonkuk Kim ^a, Changhyeon Nam ^d, Sangjoon Ahn ^d, Ju-Young Kim ^{c,*}, Hayoung Chung ^{b,*}, Jae Sung Son ^{a,*}

- a Department of Chemical Engineering, Pohang University of Science and Technology (POSTECH), Gyeongsangbuk-do 37673, Republic of Korea
- b Department of Mechanical Engineering, Ulsan National Institute of Science and Technology (UNIST), Ulsan 44919, Republic of Korea
- ^c Department of Materials Science and Engineering, Ulsan National Institute of Science and Technology (UNIST), Ulsan 44919, Republic of Korea
- d Department of Nuclear Engineering, Ulsan National Institute of Science and Technology (UNIST), Ulsan 44919, Republic of Korea

ARTICLEINFO

Keywords: Ductile semiconductor Thermoelectric material Auxetic metamaterials Power generator 3D printing

ABSTRACT

Sustainable energy solution has resulted in significant interest in thermoelectric power generation, converting waste heat into electricity. However, the practical application of thermoelectric generators has been hindered by issues with their adaptability to arbitrary heat sources and durability in an operational environment. Here, we propose deformable auxetic thermoelectric metamaterials composed of high-entropy (Ag,Cu)₂(S,Se,Te) ductile alloys, realized using finite element modelling and three-dimensional (3D) printing. We design a re-entrant auxetic structure with a negative Poisson's ratio to maximize the mechanical deformability and develop an (Ag,Cu)₂(S,Se,Te) particle-based colloidal 3D printable ink, tailored with Te microparticles. The 3D-printed (Ag,Cu)₂(S,Se,Te) alloy exhibit a *ZT* value of 1.15 coupled with high compressive strength (208 MPa) and fracture strain (17.5%). The fabricated auxetic metamaterials exhibit excellent vibrational stability and adaptability to diverse curved surfaces, realizing efficient power generation on a synclastic curved heat source. Our approach offers a method to design durable and efficient heat recovery devices.

1. Introduction

Thermoelectric (TE) power generation, which converts waste heat into electricity, has attracted considerable attention as a solution to worldwide concerns related to the depletion of fossil fuels and the need for a sustainable energy supply [1–3]. The energy-conversion efficiency of TE generators (TEGs) depends on the efficiency of the TE material and the temperature difference across the TEGs [4]. To achieve high performance of TEGs, studies have focused on improving the TE material efficiency [5–7], which is estimated by the dimensionless figure of merit ($ZT = S^2 \sigma T/\kappa$), where S is the Seebeck coefficient, σ is the electrical conductivity, κ is the thermal conductivity, and T is the absolute temperature. However, sustainable energy recovery by TE power generation in real operational environments necessitates the consideration of additional external factors, including adaptability to the dynamic surfaces of heat sources for efficient heat transfer and durability in real

operational environments. The most relevant heat sources possess curved surfaces (observed in components such as exhaust pipes and heat exchangers) and are often operated under unavoidable mechanical vibrations [8,9]. However, traditional TE legs in a device are manufactured via zone melting- and hot-pressing-based synthesis of ingots and subsequent dicing, which restricts the geometry of TEGs to a typical planar layout. These stereotypical devices yield poor performance owing to ineffective heat transfer from the non-conformal interfacial contact on the arbitrary surfaces of the heat sources [10]. Moreover, the inherent brittleness of state-of-the-art TE materials (e.g. Bi₂Te₃, PbTe, and SnSe) accelerates the failure of TEGs with repetitive exposure to mechanical vibrations [11–13]. One potential solution to these issues involves maximizing the deformability of inorganic TE materials without the degradation of materials' efficiency, enabling their adaptation to arbitrary and dynamic surfaces, and increasing their tolerance to mechanical vibrations.

E-mail addresses: juyoung@unist.ac.kr (J.-Y. Kim), hychung@unist.ac.kr (H. Chung), sonjs@postech.ac.kr (J.S. Son).

^{*} Corresponding authors.

 $^{^{1}\,}$ These authors contributed equally to this work.

Mechanical metamaterials are artificial materials with excellent mechanical properties [14]. They exhibit unique properties owing to the topology of the designed representative units rather than the inherent properties of their constituent materials. Consequently, they have a diverse array of applications including strain sensing, smart filters, vibration damping, protective devices, and heat exchangers [15]. In mechanical metamaterials, auxetic metamaterial is the most widely used structure, which is intentionally designed to possess a negative Poisson's ratio (NPR, v < 0) that is rarely found in natural materials [16]. Auxetic metamaterials can simultaneously expand in both the lateral and perpendicular directions under tensile forces, and contraction when subjected to compression along the corresponding direction [17]. This unique deformation behavior facilitates adaptation to a wide range of complex and dynamic surfaces and exhibits several desirable mechanical properties, including superior shear resistance, indentation resistance, fracture resistance, synclastic behavior, variable permeability, and better energy absorption performance [18-21].

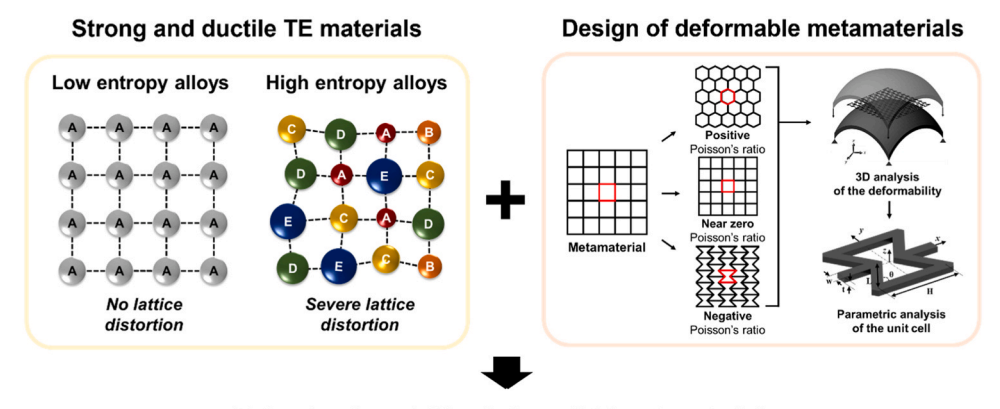
Ag₂S-based compounds have emerged as a novel class of ductile semiconductors, sparking significant research efforts toward their application as semiconductors in deformable electronic and TE devices [22–26]. Recently, high-entropy alloy engineering in ductile compounds such as (Ag,Cu)₂(S,Se,Te) has been reported to bolster both strength and ductility through solid solution strengthening, while enhancing TE efficiency, thus providing an excellent model material for diverse structural designs for deformable and efficient TE devices [27,28]. Herein, we present a structural design strategy for auxetic metamaterials comprising high-entropy (Ag,Cu)₂(S,Se,Te) ductile TE materials using three-dimensional (3D) finite element method (FEM) simulations and experimental validation of the design using extrusion-based 3D printing process (Fig. 1). We developed comparative FEM models of the re-entrant auxetic, honeycomb, and lattice structures to evaluate the mechanical deformability of TE metamaterials and conducted a parametric study for identifying the best-performing auxetic structures. The 3D-printed (Ag,Cu)₂(S,Se,Te) high-entropy alloy exhibited a maximum ZT value of 1.15 at 950 K, coupled with a synergistic enhancement in the mechanical strength and ductility. The designs were validated by comparatively evaluating the bending deformability of 3D-printed metamaterials on complex curved surfaces of monoclastic, synclastic, and monkey saddle structures and their vibrational stability, where the auxetic structures demonstrated superior deformability and stability. Finally, the fabricated auxetic TEG, conformably mounted on a synclastic curved heat source, exhibited a power density of 6.3 mW cm⁻² at a temperature difference of 155 K, thus validating our approach for improving the adaptability and durability of TEGs for arbitrary heat sources.

2. Results and discussion

2.1. Design of deformable auxetic TE metamaterials

To design a topology of metamaterials with high adaptability to complex curved surfaces, we developed 3D finite element analysis (FEA) models of three designs with re-entrant auxetic, lattice, and honeycomb structures having negative, near-zero, and positive PR, respectively. To solely focus on the deformation mechanism of each metamaterial, we conducted the 3D finite element analysis at room temperature. We quantified the degree of conformity through the von Mises stress induced when metamaterials were completely attached (i.e., without a gap) to a curved rigid surface with curvatures ranging between 1/100 and 1/40 (Fig. 2a, Fig. S1). The von Mises stress is a widely used failure criterion that considers all the applied stresses on the object [29]. In all cases, the auxetic structure exhibits the lowest stress (Fig. 2b); e.g., approximately 39 % and 82 % lower stresses than that in the lattice and the honeycomb structures were predicted on the surface with the curvature of 1/40. Notably, although the stress is concentrated at the hinges that connect the struts and the maximum stresses are found therein regardless of the type of metamaterial, the overall stress distribution within the structure is smoother in the auxetic structure compared to other metamaterials.

Such an enhancement of conformity to the curved domain found in



Extrusion-based 3D printing of TE metamaterials

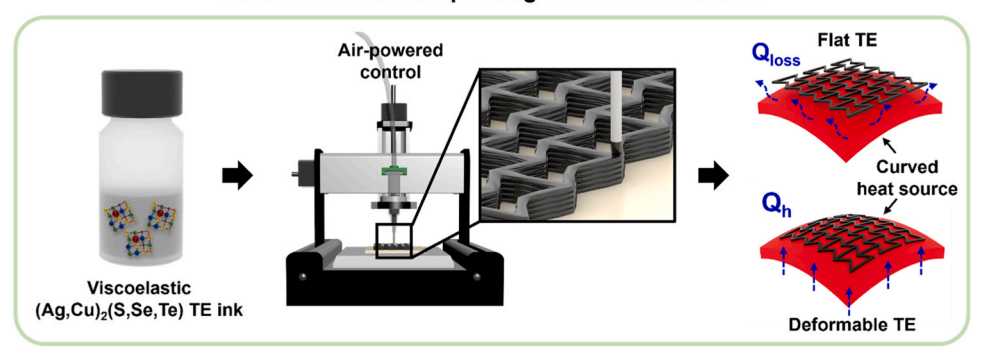


Fig. 1. Scheme of high entropy engineering and structural design for the development of a deformable TEG using extrusion-based 3D printing.

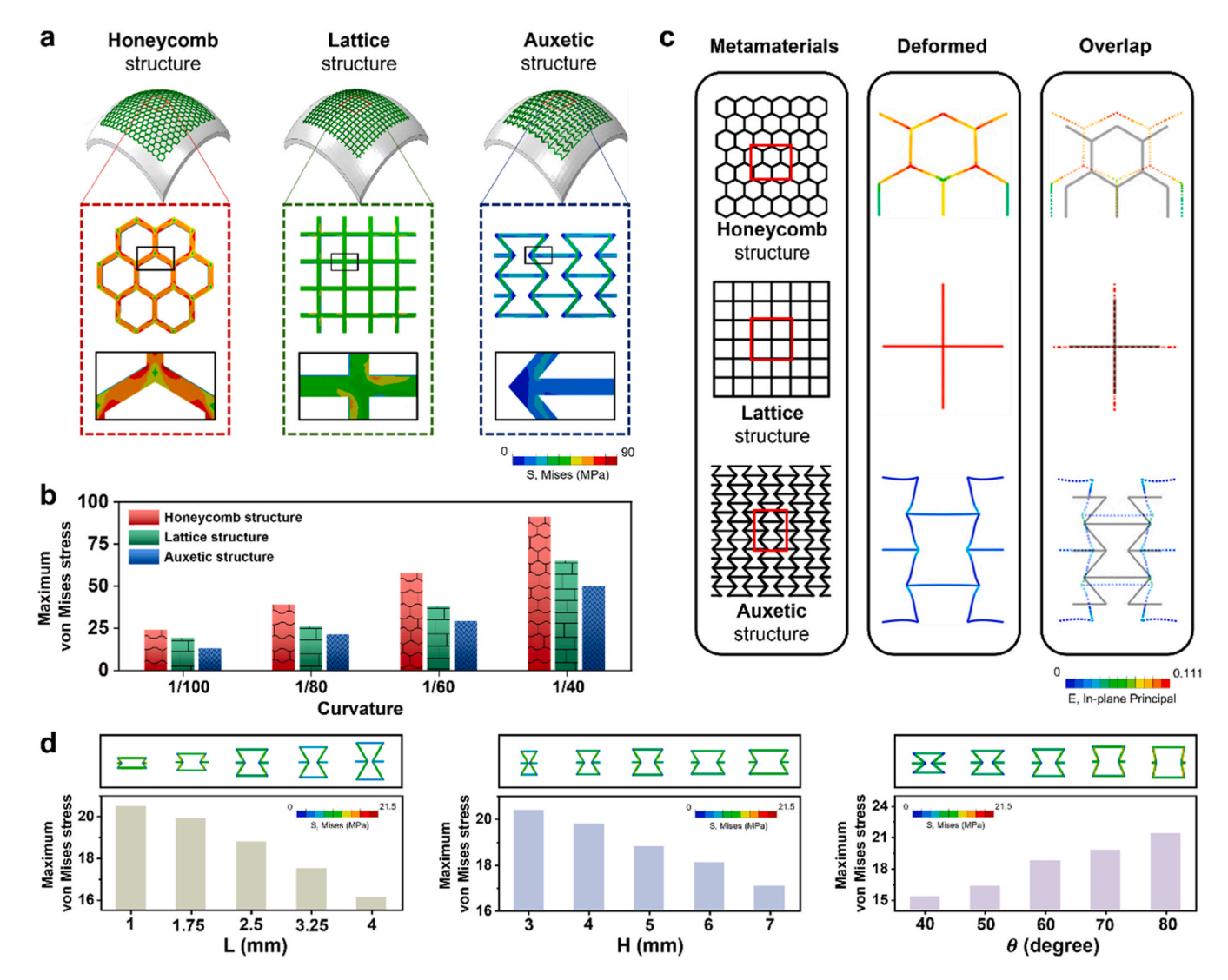


Fig. 2. Design of deformable auxetic TE metamaterials. (a) Three-dimensional (3D) analysis on the deformability of metamaterials showing von Mises stress distribution of the honeycomb, lattice, and auxetic structure attached onto the curved surface with synclastic curvature of 1/40. (b) Maximum von Mises stresses of the honeycomb, lattice, and auxetic structure attached onto the various curved surfaces with synclastic curvature ranging from 1/100-1/40. (c) 2D Two-dimensional analysis of the fundamental deformation mechanisms in metamaterials with respect to the Poisson's ratio of each structure. (d) Parametric study of the geometrical parameters (H, L, θ) for the enhanced deformability of the re-entrant structure on a synclastic surface, based on the maximum von Mises stress within each representative volume element.

the auxetic metamaterial can be attributed to the fundamental mechanism of auxetics, which is illustrated by the deformation of the simplified truss network models (Fig. 2c). Although considerably simplified, the network model can capture the difference in deformation mechanisms between the metamaterials when their representative unit cells are subjected to isotropic eigenstrain (i.e., $\epsilon_{xx} = \epsilon_{yy}$). The auxetic structure resulted in the lowest principal strain compared with the other metamaterials, which can be attributed to the unique deformation mechanism comprising substantial rigid body rotations of the beams associated with the NPR. Consequently, a non-affine displacement field was found in the auxetic structure, as shown in Fig. 2c. In contrast, the honeycomb and lattice structures, which exhibited affine displacement, demonstrated a higher strain distribution across the entire structure.

Further, a simulation-based parametric optimization of the geometric configuration was conducted for optimal conformity of the reentrant auxetic structure (Fig. 2d). We considered the geometrical parameters H,L, and θ , which are the horizontal wall length, the inclined wall length, and the inclination angle, respectively, to conduct a parametric study (Fig. 1). Considering the printing capabilities of the 3D printing and the materials used in this study, we set H=5 mm,

L=2.5 mm, and $\theta=60^\circ$ as the baseline configuration. An increase in the size parameters (i.e. L and H) was found to decrease the maximum stress, which is consistent with the fact that an increase in the unit cell size leads to a higher the void ratio, decreasing the specific bending rigidity in each direction [30]. However, there is still a trade-off between increasing dimensions and material strength, as the decrease in the number of unit cells adversely affects the property. Second, the stress was proportional to the angle parameter θ as the sharper corners amplified the auxetic behavior with a smaller θ , and rigid body motion of the struts was promoted during attachment. The best-performing structure was optimized to have the parameters of H=5 mm, L=2.5 mm, and $\theta=48^\circ$. This metamaterial demonstrated higher conformality with maximum von Mises stress that was approximately 17 % lower than the baseline, coupled with 16 % reduction in NPR when compared to the baseline structure.

2.2. 3D printing of the auxetic TE metamaterials

To fabricate the designed auxetic TE metamaterials, we conducted extrusion-based 3D printing of viscoelastic TE inks containing

Ag_{0.1}Cu_{1.9}S_{0.25}Se_{0.25}Te_{0.5} TE particles, tailored with a Te additive. Highentropy Ag_{0.1}Cu_{1.9}S_{0.25}Se_{0.25}Te_{0.5} were synthesized using mechanical alloying. X-ray diffraction (XRD) patterns of the synthesized particles indicated that the peaks shifted from the reference pattern of the Cu₂Te hexagonal structure (Fig. 3a), and no additional peaks related to the secondary phase or impurities were observed. This structural behavior agrees well with the reported pattern of the high entropy alloy of (Ag, Cu)₂(S,Se,Te) synthesized by the melting method [27]. Considering the limited theoretical solubility (no more than 0.01) of Ag in Cu₂Te, the formation of this single-phase structure can be attributed to the increased configurational entropy of the Ag_{0.1}Cu_{1.9}S_{0.25}Se_{0.25}Te_{0.5} TE particles [27].

The high viscoelasticity of colloidal inks is essential for ensuring smooth flow through nozzles and maintaining the structural integrity of the printed structures in the extrusion-based 3D printing process [31]. Ball-milled Te microparticles with the negative surface charges were used as additives to achieve the desired viscoelastic properties and marked improvement in colloidal stability in the Ag_{0.1}Cu_{1.9}S_{0.25}Se_{0.25}Te_{0.5} colloid-based inks by the electrostatic interaction (Fig. 3b–d, Fig. S2) [10,32–35]. The negative surface charge of Te microparticles can be attributed to the high electronegativity of chalcogen elements, which tend to draw electrons towards themselves [36–38]. Additionally, triboelectric effects during ball-milling, where friction and impact cause electron transfer, result in the accumulation of electrons on the Te particles [39,40]. The TE ink in its original state, devoid of additives, exhibited Newtonian fluid behavior with dynamic viscosity (η) of approximately 10 Pa·s (Fig. 3e). Whereas all inks with Te particles

exhibited enhanced η' and negative dependencies on the shear rate, being indicative of a Bingham fluid. The Bingham fluid implies a 3D network in a colloidal system undergoing shear stress-induced collapse, which results in a sudden decrease in viscosity decrease Fig. S3) [41].

The excellent viscoelasticity of the Ag_{0.1}Cu_{1.9}S_{0.25}Se_{0.25}Te_{0.5}/Te₂₀ TE inks enabled the creation of complex structures via direct 3D writing, including a freestanding arch-type architecture (inset in Fig. 3 f), highaspect-ratio filaments ranging as 2.7-12.5 (Fig. 3 f), and diverse metamaterials (Fig. 3 g, i-p, Video S1). The printed samples were sintered using a two-step heat treatment at 1003 and 1123 K. At 1003 K, the liquified Te, with a melting point of 723 K, permeated and filled the pores and voids between the TE particles, inducing liquid-phase sintering of the product (Fig. S4). In liquid-phase sintering, uniform distribution and homogeneous melting of the liquified phase are essential for effective densification during liquid-phase sintering. Our findings indicate that heat treatment at 1003 K is the optimal condition for the homogeneous distribution of liquified Te. When the temperature is directly increased to 1123 K, the liquified Te fails to distribute evenly and is expelled from the samples, as evidenced in the photograph (Fig. S5). Conversely, at temperatures below 1003 K, densification is not effectively promoted, resulting in insufficient sample density. The printed samples were further annealed at 1123 K for the desired duration to promote densification and to improve thermoelectric properties by regulating carrier concentration through the evaporation of excess Te. At temperatures below 1123 K, the Te evaporation rate is significantly slower, necessitating prolonged durations to achieve the desired carrier concentrations. Scanning electron microscopy (SEM) images of

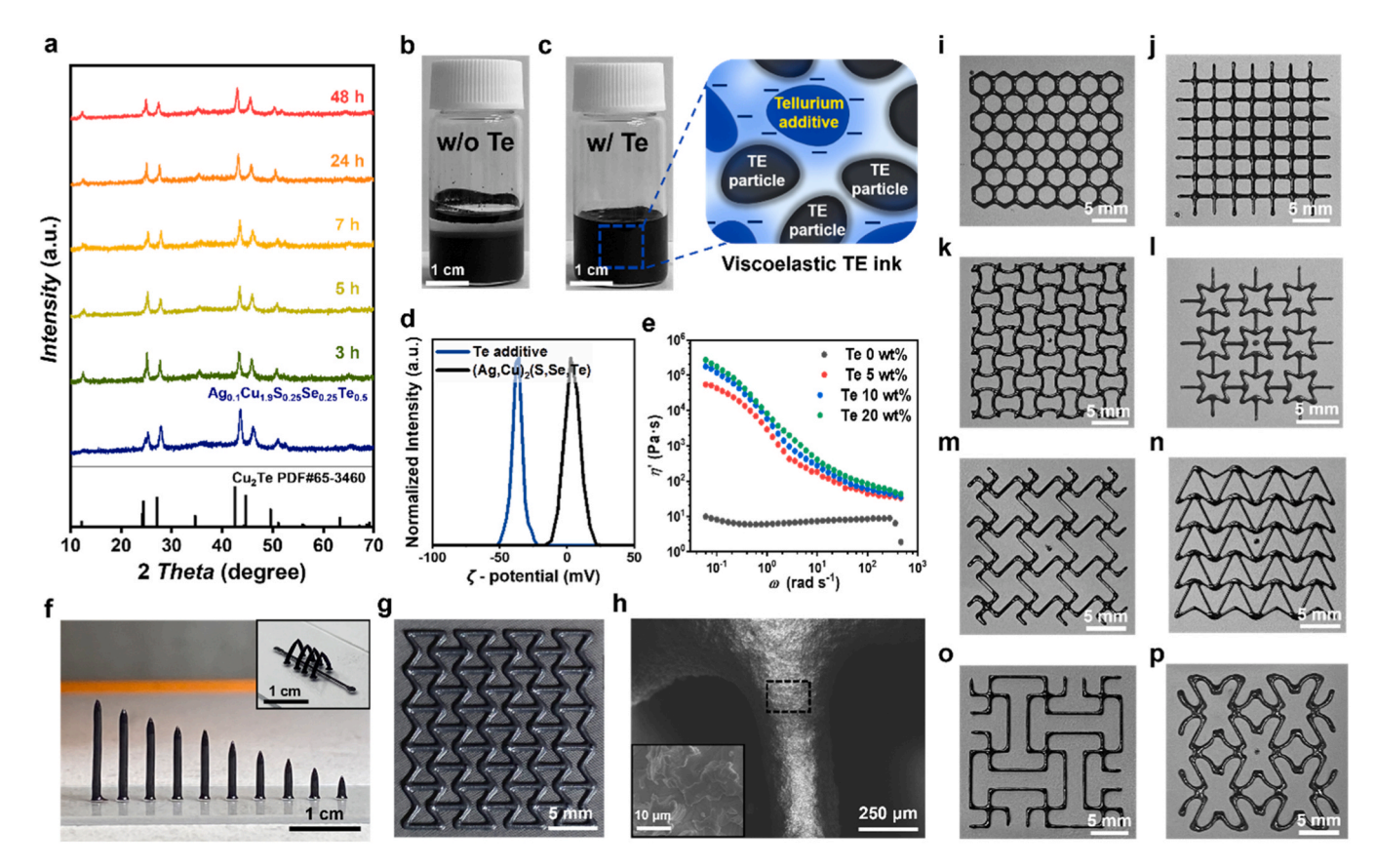


Fig. 3. 3D printing of $(Ag,Cu)_2(S,Se,Te)$ TE auxetic metamaterials. (a) XRD patterns of as-synthesized $Ag_{0.1}Cu_{1.9}S_{0.25}Se_{0.25}Te_{0.5}$ powder and sintered samples for 3, 5, 7, 24 and 48 h for 1123 K. Photographs showing (b) TE ink containing only TE particles and (c) viscoelastic TE ink with Te additives. Both represent the state after 10 days of ink synthesis. (d) The ζ potential curves of Te additives and $Ag_{0.1}Cu_{1.9}S_{0.25}Se_{0.25}Te_{0.5}$ particles in colloids. (e) Dynamic viscosity (η') of $(Ag,Cu)_2(S,Se,Te)$ TE inks with various Te additive contents. (f) Photographs showing 3D filaments with different aspect ratios (2.7–12.5) and arch-type architecture (inset). (g) Photograph of the 3D-printed re-entrant auxetic metamaterial. (h) SEM image of the sintered re-entrant auxetic metamaterial for 24 h. The inset shows the corresponding high-resolution SEM image. Photographs showing various 3D-printed metamaterials: (i) Honeycomb, (j) lattice, (k) sinusoidal ligaments, (l) star honeycomb, (m) structurally hexagonal re-entrant honeycomb, (n) double arrowhead, (o) lozenge grids, and (p) S-shaped structures.

the sintered samples (inset in Fig. 3H, Fig. S6) exhibited well-sintered grains in all the samples, regardless of the sintering duration. Although the formation of sub-10 µm-scale pores among grains were observed in all samples, the porosity was progressively reduced by extending the sintering duration. This result was further supported by the relative densities of the samples, which increased from 83 % to 95 % as the sintering time increased from 3 to 48 h (Fig. S7). During the sintering step, we observed a significant volume shrinkage of approximately 50 %, indicating the efficient sintering of TE particles (Fig. S8). Additionally, the energy dispersive spectroscopy (EDS) mapping images of the samples sintered for 24 h at 1123 K showed a homogeneous distribution of all the elements in the entire structure without any phase separation (Fig. S9). Similar to the synthesized TE particles, the XRD patterns of the printed and sintered samples exhibited peaks that were shifted from those of the Cu₂Te reference. With increase in the sintering duration, the peaks corresponding to the hexagonal phase progressively shifted to lower angles, which can be attributed to the solid-state reaction of excess Te with the (Ag,Cu)₂(S,Se,Te) matrix during the sintering process (Fig. 3a, Fig. S10).

Supplementary material related to this article can be found online at doi:10.1016/j.nanoen.2024.110392.

Despite sintering shrinkage, the primary printing architectures at the macroscale were well conserved (Fig. 3h, Fig. S11). Various metamaterial architectures maintained their designed structures during sintering, and no structural distortion was observed. Owing to the high reproducibility of this sintering shrinkage rate, the computer-aided design model can be scaled before printing to ensure the production of the desired architecture.

2.3. TE properties of the 3D-printed (Ag,Cu)₂(S,Se,Te)

In the realm of copper-chalcogenide-based TE materials, the controlled formation of Cu vacancies is crucial for optimizing the TE properties because Cu vacancy defects act as hole donors [42]. To regulate the content of Cu vacancies in the 3D-printed (Ag,Cu)₂(S,Se, Te), we varied the sintering duration at 1123 K, at which the excess Te could be evaporated and the formation of Cu vacancies was

consequently reduced. Hall measurements were conducted to investigate the carrier concentration ($n_{\rm H}$) and hole mobility ($\mu_{\rm H}$) for printed samples with different sintering duration (Fig. 4a). As predicted, the room temperature $n_{\rm H}$ in the printed samples decreased from 3.67 × 10²⁰ to 17.9 × 10²⁰ cm⁻³ as the sintering duration increased from 3 to 48 h at 1123 K. Additionally, the $\mu_{\rm H}$ showed an increase from 2.33 to 4.34 cm² V⁻¹ s⁻¹ with longer sintering duration. The increase in the $\mu_{\rm H}$ can be explained by the reduction in the defect density and the concurrent increase in sample density (Fig. S7). The markedly low $\mu_{\rm H}$ (< 5 cm² V⁻¹ s⁻¹) in all samples, compared to Cu₂Te with 13 cm² V⁻¹ s⁻¹, can be understood based on the alloy scattering, severe lattice disorder and lattice defects, which is a common trait of high-entropy materials [43, 44].

We measured the temperature-dependent TE properties of the (Ag, Cu)₂(S,Se,Te) samples sintered at 1123 K for 3, 5, 7, 24, and 48 h across the temperature range of 300–950 K. The electrical conductivities of all samples were fluctuated at approximately 400 and 750 K, being attributed to the phase transition (Fig. 4b) [27]. The temperature dependence of the Seebeck coefficients in all the samples was positive over the entire temperature range (Fig. 4c). The room-temperature electrical conductivity gradually decreased and the Seebeck coefficient increased with increasing sintering duration. This trend aligns with the changes in $n_{\rm H}$. Owing to the high Seebeck coefficients, the power factors were generally increased when extending the sintering duration in the entire temperature range, where the highest power factor of 8.01 μ W•cm⁻¹ K⁻² was achieved by the 48h-sintered sample at 950 K (Fig. 4d).

Fig. 4e presents the temperature dependent thermal conductivity (κ) for (Ag,Cu)₂(S,Se,Te) samples. The 48h-sintered sample exhibited the lowest κ of 0.40 W•m⁻¹•K⁻¹ at 350 K, which was only approximately 20 % of the reported value of bulk polycrystalline Cu₂Te materials [42, 45]. To understand this low κ , we calculated the lattice thermal conductivities (κ _L) of all samples by subtracting the κ _e from the total thermal conductivity; κ e was estimated by using the Wiedemann-Franz relationship (κ _e = $L\sigma T$), where L is the Lorenz number obtained by the single parabolic band model (Fig. S12) [46]. Subsequently, the calculated κ _L exhibited remarkably low values below 0.5 W•m⁻¹•K⁻¹, primarily attributed to the reduction in electronic thermal conductivity resulting

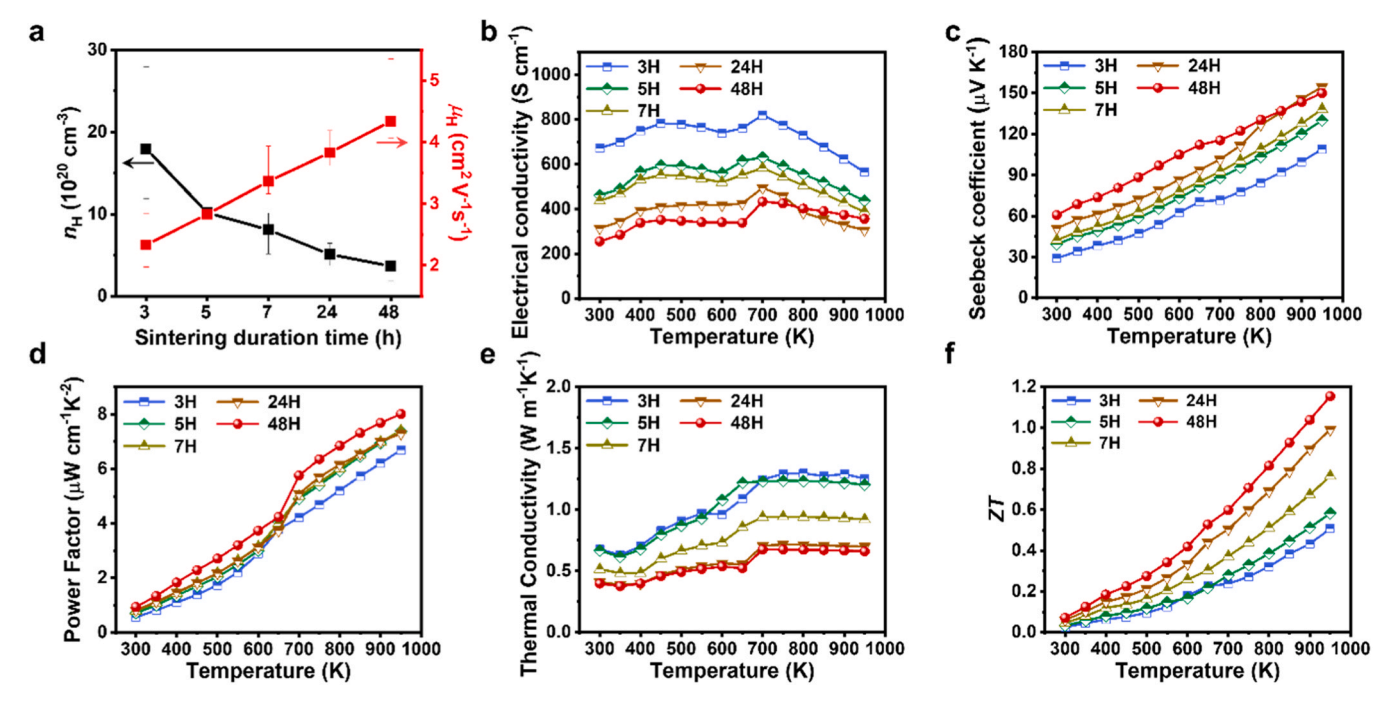


Fig. 4. TE properties of the 3D-printed $(Ag,Cu)_2(S,Se,Te)$ materials. (a) Room-temperature carrier concentrations and mobilities of the $(Ag,Cu)_2(S,Se,Te)$ samples as a function of sintering times at 1123 K. Temperature dependent (b) electrical conductivities, (c) Seebeck coefficients, (d) power factors, (e) thermal conductivities, and (f) ZT values for the $(Ag,Cu)_2(S,Se,Te)$ samples sintered for 3, 5, 7, 24, and 48 h at 1123 K.

from a decrease in carrier concentration due to Te evaporation during heat treatment. (Fig. S12–13) [7,27,28]. Consequently, the maximum ZT value was achieved by the 48h-sintered sample with 1.15 at 950 K (Fig. 4f), which indicated an improvement of 230 % over that of polycrystalline Cu₂Te (ZT=0.5) [45] and close to the reported value of the similar composition of a Cu₂Te-based high entropy alloy [27]. This maximum ZT value is one of the highest among the reported ductile inorganic materials (Fig. S14).

2.4. Mechanical properties of the 3D-printed (Ag,Cu)₂(S,Se,Te)

The realization of high deformability inherent in auxetic structures necessitates materials with enhanced mechanical ductility. In this study, compressive stress-strain tests were conducted on 3D-printed (Ag, Cu)₂(S,Se,Te) samples sintered for varying durations of 3, 5, 7, 24, and 48 h (Fig. 5a). Extended sintering durations resulted in a notable enhancement of compressive strength and fracture strain (Table S1) due to the densified microstructures of the samples (Fig. 5c, d, Fig. S5). Prolonged sintering duration contributed to a more annealed microstructure, emphasizing strain-hardening through dislocation multiplication, thereby leading to elevated compressive fracture strength and strain. Furthermore, the compressive strengths and porosities of the sintered samples exhibited a linear correlation (Fig. S15). The decrease in porosity correlates with an increase in compressive strength, aligning well with the Hasselmann model [47]. This trend is attributed to the adverse impact of pores or voids on the quantity of the solid material, compromising the overall structural integrity [48].

Under the optimum condition, the $(Ag,Cu)_2(S,Se,Te)$ sample sintered for 24 h exhibited a compressive strain of 17.5 % and a compressive strength of 208 MPa. As control samples, stress-strain tests were conducted on 3D-printed TE materials, including $(Bi,Sb)_2Te_3$, Na-doped PbTe, Sb-doped PbTe, and Cu_2Se [34], following reported methods. Notably, the 3D-printed $(Ag,Cu)_2(S,Se,Te)$ TE materials displayed

significantly greater plasticity, compressive strength, and energy absorption, as depicted in Fig. 5b. These superior mechanical properties can be attributed to the unique intrinsic ductile properties of Ag_2S -based alloys and the principles of high-entropy engineering.

Further, we conducted the bending tests on cuboid-shaped and auxetic structure samples (Fig. S16). The bending tests showed that cuboid-shaped samples had a bending strain of approximately 0.8 %. This relatively low bending strain can be attributed to the internal porosity, which acts as stress concentrators, reducing the material's overall ability to withstand bending forces. In contrast, the auxetic structure samples achieved a maximum bending strain of 3.26 %, which is more than four times greater than that of the cuboid samples, and this was achieved with much less applied stress. This indicates that the auxetic design allows for better stress distribution and absorption, mitigating the adverse effects of internal porosity. The substantial improvement in bending strain clearly demonstrates the effectiveness of structural design in enhancing the mechanical properties of TE printing materials.

The distinctive ductility of the printed $(Ag,Cu)_2(S,Se,Te)$ was further substantiated by microstructural changes observed during deformation. In the inset images of Fig. 5a, the 24h-sintered sample exhibited evident swelling prior to fracture, indicative of plastic deformation in ductile materials. Additionally, post-compressive testing revealed multiple shear bands on the sample's surface (Fig. 5e, Fig. S17). The interaction and intersection of these shear bands effectively increased the flow stress, facilitating shear branching and rotation until fracture, thereby contributing to the observed the high compressive strength and ductility of the materials [49]. Comparative analysis with reported properties of Bi₂Te₃ [11], PbTe [12], SnSe [13], and Cu₂Te crystals [27,50], as well as ductile Ag₂S-based families [24–26], reveals higher compressive strength and fracture strain in our (Ag,Cu)₂(S,Se,Te) samples (Fig. 5f). This simultaneous enhancement in mechanical strength and ductility may be attributed to the solid solution strengthening effect induced by

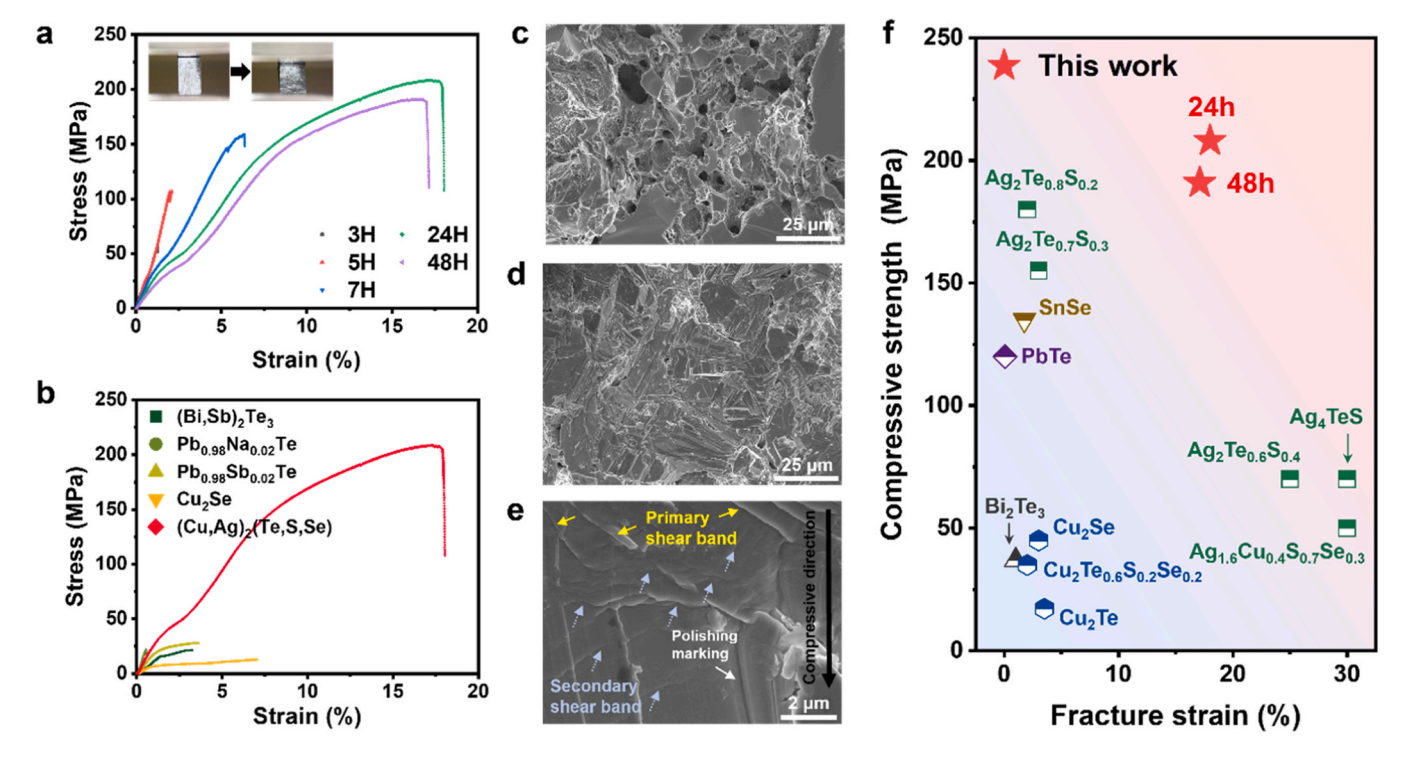


Fig. 5. Mechanical properties of the 3D-printed $(Ag,Cu)_2(S,Se,Te)$ materials. (a) Compressive stress-strain curves of the $(Ag,Cu)_2(S,Se,Te)$ samples sintered for 3, 5, 7, 24, and 48 h at 1123 K. The inset shows a cuboid of $(Ag,Cu)_2(S,Se,Te)$ samples sintered for 24 h, for the compression test (left) and its deformation under compression (right). (b) Comparison of compressive stress-strain curves with the previous reported 3D-printed state-of-the-art TE materials. SEM images of fractured surfaces of the $(Ag,Cu)_2(S,Se,Te)$ samples sintered for (c) 0 h and (d) 24 h at 1123 K. (e) SEM image of the surface of the $(Ag,Cu)_2(S,Se,Te)$ sample sintered for 24 h after compression test. (f) Compressive strength versus the fracture strain for $(Ag,Cu)_2(S,Se,Te)$ samples and other representative inorganic TE materials.

high entropy alloying. Previous study has demonstrated the synergistic effect achieved through the incorporation of Ag into Cu₂(S,Se,Te) via entropy engineering [27], leading to significant lattice distortion, hindering dislocation migration, and enhancing mechanical strength while inducing notable plastic deformation in the (Ag,Cu)₂(S,Se,Te) TE material [51]. These improved mechanical properties offer flexibility in various structural designs, resulting in superior mechanical behaviors.

2.5. Deformability and durability of $(Ag,Cu)_2(S,Se,Te)$ auxetic metamaterials

We assessed the deformability of 3D-printed (Ag,Cu)₂(S,Se,Te) auxetic metamaterials through a bending test, subjecting samples to curved surfaces. The 3D-printed auxetic structures exhibited versatile adaptability, seamlessly conforming to monoclastic and synclastic curvatures, as well as the monkey saddle structure (Fig. 6a-d). We further conducted a comparative deformability test on three designs of the auxetic structure, alongside 3D-printed lattice and honeycomb structures as control samples, onto synclastic surfaces with curvatures ranging from 1/80–1/40. (Fig. 6e). As anticipated, the auxetic structure deformed without cracks across all the curvatures. Conversely, the lattice structure, with a near-zero Poisson's ratio, exhibited cracks beyond a curvature of 1/60. Furthermore, the honeycomb structure, with a positive Poisson's ratio, experienced failure at a more modest curvature of 1/70. This observation aligns with trends of the maximum Von Mises stresses at various curvatures shown in the FEM simulations (Fig. 2b), underscoring the superior deformability of the auxetic structure with an overall lower maximum von Mises stress.

To assess the durability of the deformable TE materials under practical vibrational conditions, we conducted vibration tests on 3D-printed

(Ag,Cu)₂(S,Se,Te) and (Bi,Sb)₂Te₃, both featuring auxetic structures (Fig. 6f, g). Although (Bi,Sb)₂Te₃ is a widely used TE material at room temperature, its inherent brittleness and limited deformability pose challenges [52]. The deformable (Ag,Cu)₂(S,Se,Te) auxetic metamaterials exhibited high vibrational stability for cycles up to 5.4×10^4 times. In contrast, (Bi,Sb)₂Te₃ auxetic metamaterials failed to maintain their original structures under vibrational stress, with the continuous microcrack generation causing structural failure after 3.6×10^4 cycles. Despite the enhancement in the overall structural characteristics through design, the exceptional mechanical properties of the material itself are crucial, emphasizing the synergistic effects of incorporating both robust and ductile TE material and structural design in this study.

2.6. Power generation of the auxetic TEG on a synclastic heat source

To evaluate the practical application potential of the auxetic TE metamaterials, we fabricated a prototype deformable TEG composed of a re-entrant unit cell with the optimized configuration and attached it on a curved heat source with a synclastic curvature of 1/40 (Fig. 7a). As the hot-side temperature gradually increased, the auxetic TEG reached a maximum temperature difference of approximately 155 K (Fig. S18). Temperature differences were uniformly created over the entire range of the auxetic structure, irrespective of position (Fig. S17) owing to the conformance and stable thermal contact. With the increasing temperature difference, the output voltage increased linearly, while the output power density exhibited a quadratic increase, resulting in values of 12.8 mV and 6.29 mW cm⁻² (Fig. 7b, Fig. S20). The observed output voltage and power were slightly higher than the calculated values, particularly at elevated temperatures. This discrepancy may be attributed to measurement errors, likely caused by slight deviations between

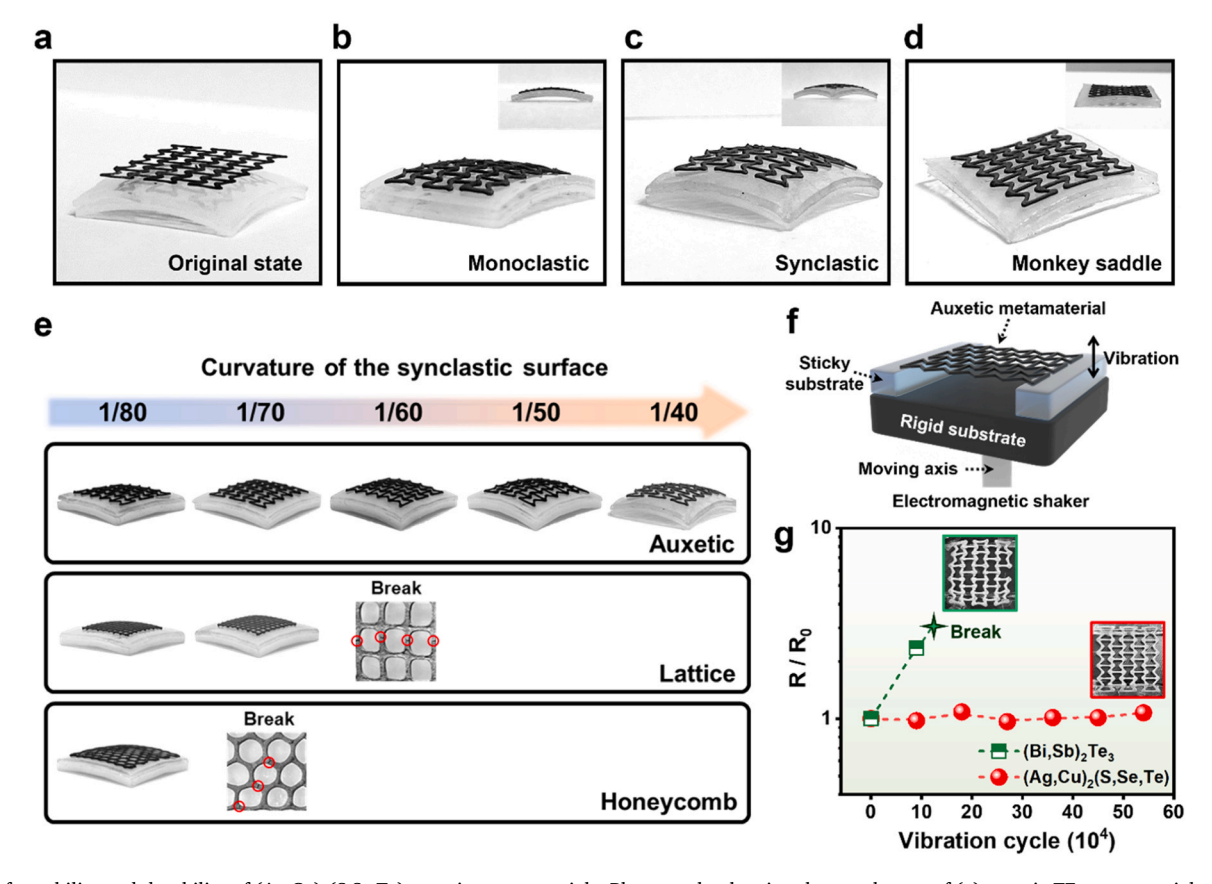


Fig. 6. Deformability and durability of $(Ag,Cu)_2(S,Se,Te)$ auxetic metamaterials. Photographs showing the attachment of (a) auxetic TE metamaterials to intricate surfaces with (b) monoclastic and (c) synclastic curvatures, and (d) a monkey saddle structure. (e) Deformability test of auxetic, lattice, and honeycomb metamaterials onto the synclastic surfaces with curvatures ranging from 1/80-1/40. (f) Schematic illustration showing the vibration test. (g) Comparison of resistance changes in $(Ag,Cu)_2(S,Se,Te)$ and $(Bi,Sb)_2Te_3$ auxetic metamaterials during vibration tests, as a function of vibration cycles.

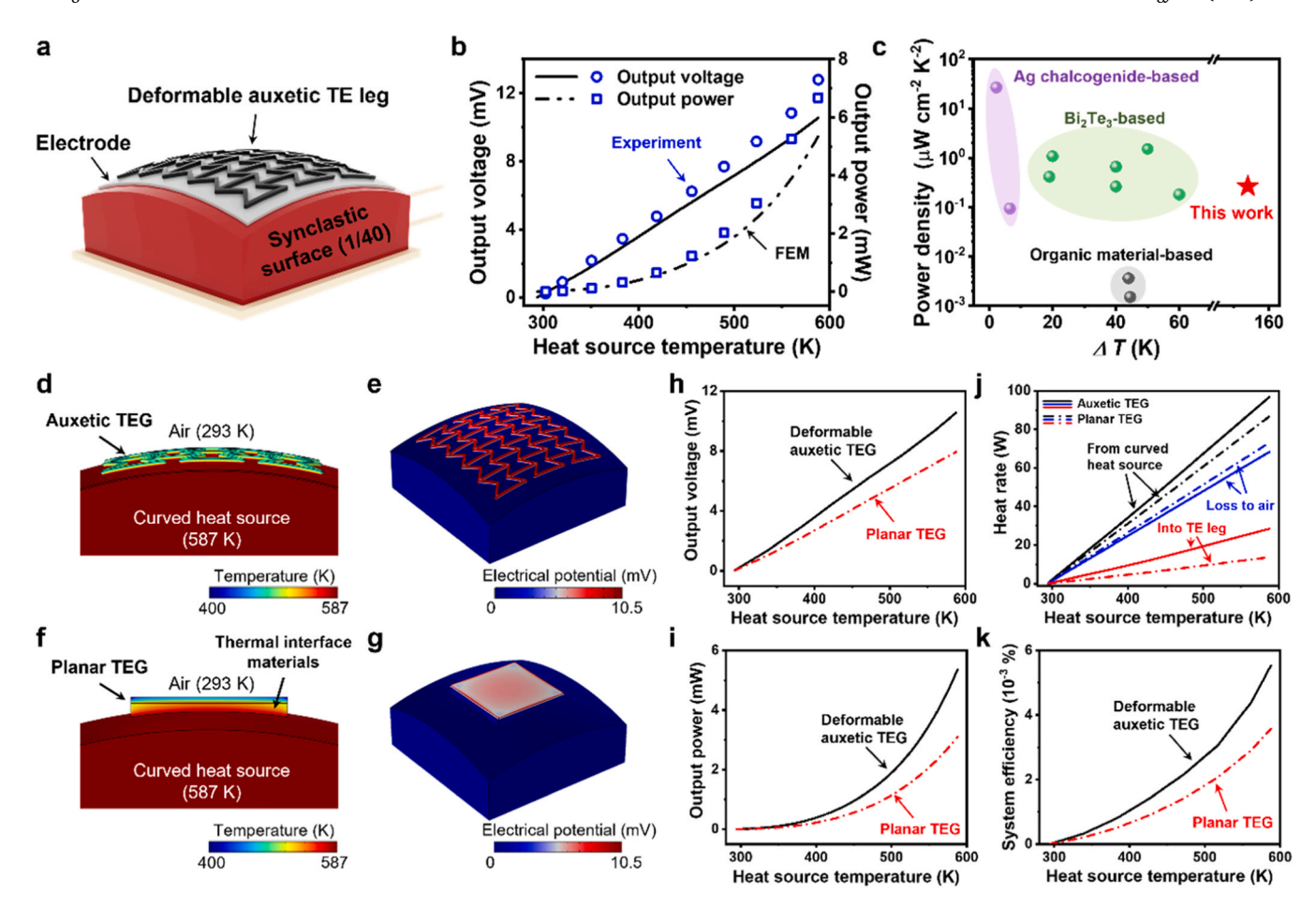


Fig. 7. Power generation of deformable $(Ag,Cu)_2(S,Se,Te)$ auxetic metamaterials. (a) Schematic illustration showing the deformable auxetic TEG positioned on a synclastic surface with a curvature of 1/40. (b) The output voltage and output power of the deformable auxetic TEG as a function of the heat source temperature obtained by FEM (line) and experiment (symbol). (c) Comparison of the temperature difference-normalized power densities of stretchable TE modules reported under energy harvesting conditions. Schematics showing (d) the temperature distribution and (e) the electrical potential of the deformable auxetic TEG, calculated by the FEM. Schematics showing (f) the temperature distribution and (g) the electrical potential of the planar TEG, calculated by the FEM. Calculated (h) output voltage, (i) output power, (j) heat rate, and (k) system efficiency of the deformable auxetic TEG and the planar TEG as a function of the heat source temperature.

the thermocouple readings and the actual material temperature. The temperature difference-normalized power density of the 3D-printed (Ag, $\text{Cu})_2(S,\text{Se},\text{Te})$ material exhibits the comparable values to the reported inorganic-based deformable TEGs and higher than organic-based deformable TEGs. Additionally, our auxetic TEGs offer a notable advantage, compared with others, in terms of wide operable temperatures, thereby enhancing its suitability for applications requiring stable performance under varying thermal conditions.

The power density of the auxetic TEG is comparable to or higher than those of previously reported state-of-the-art deformable TEGs comprising Ag_2S -based ductile materials [23,53], organic materials [54,55], and Bi_2Te_3 -based materials with stretchable electrodes (Fig. 7c) [56–61]. Moreover, the inorganic-based auxetic TEG operated stably at 587 K with a notable temperature gradient of 155 K, which markedly exceeds the temperature distribution ranges observed in the reported stretchable TEGs with organic components.

For comparing the auxetic TEG with the typical planar TEGs, we developed 3D FEM models for predicting their power generation performances under the condition of the fixed hot-side temperature of the synclastic surface and the convection cooling of the cold side. The planar TEG was attached onto a synclastic surface using thermal interface materials with a thermal conductivity of 3 W m $^{-1}$ K $^{-1}$. The temperature and electrical potential distributions were homogeneously created across the auxetic TEG in the entire region (Fig. 7d–e), whereas the complex lateral and vertical gradients in the temperature and potential

profiles were observed in the traditional planar TEG (Fig. 7f, g). This inhomogeneity in temperature distribution could lead to the loss of heat to convert electricity, as observed in the lower output voltage in the planar TEG (Fig. 7h). Accordingly, the auxetic TEG exhibited an approximately 70 % rise in output power and up to 50 % higher system efficiency compared with those of the planar TEG when the heat source temperature reached 587 K (Fig. 7i, k). On the other hand, we further conducted the FEM simulation under the boundary condition of the fixed heat transfer rates from a heater. Like the fixed hot-side temperature condition, the deformable auxetic TEG exhibited 20 % larger output power and 12 % higher system efficiency than those of the planar TEGs (Fig. S21).

The heat from the synclastic heat source was transferred to either the TEG or dissipated to the air. The auxetic TEG, which can seamlessly adapt to the curved surface without any gaps, increases the heat transfer efficiency to the TEG by minimization of heat loss by dissipation and eventually enhances the power-generating performances. The heat rate calculation (Fig. 7j, Fig. S21g) shows that the calculated heat transfer efficiency for the auxetic TEG from a heat source is approximately two times higher than that for the planar TEG due to the lower heat loss, regardless of the boundary conditions, though the thermal interface materials aided heat transfer between the planar TEG and the synclastic surface. These results show the importance of the conformal thermal contact of TEGs to heat sources for minimizing heat loss at the junction, eventually demonstrating the feasibility of our structural design strategy

for enhancing power-generating performances.

3. Conclusion

This study demonstrated the feasibility of the structural design of ductile (Ag,Cu)2(S,Se,Te)-based auxetic TE metamaterials for efficient and durable TE power generation. Our design strategy utilized the NPR effect of an auxetic metamaterial, thus rendering it adaptable to the arbitrary and dynamic surfaces of various heat sources. By minimizing parasitic heat losses and maximizing the temperature difference across the TE leg, the auxetic TEG exhibited excellent power performance on synclastic curved heat sources. Moreover, the mechanical superiority of the high-entropy alloy (Ag,Cu)2(S,Se,Te) ensured effective endurance of mechanical vibrations and improved the sustainability of the power generation system. This study proposes a system-level design strategy for shape-deformable and efficient TE modules that incorporated auxetic features into the design of ductile TE legs. Furthermore, our structural design strategy can be extended to various TE materials with diverse functionalities, including electromagnetic, thermal, and optical properties. These advancements are expected to accelerate the integration of TEGs into actual operational environments with high temperatures and vibrations.

4. Materials and methods

4.1. Materials

Elemental Ag (powder, 99.9 %, Alfa Aesar), Cu (powder, 99.9 %, Alfa Aesar), S (powder, 99.998 %, Sigma-Aldrich), Se (powder, 99.999 %, Alfa Aesar), and Te (granule, 99.999 %, 5 N Plus) were used for high-energy ball-milling. Glycerol (>99.5 %, Sigma-Aldrich) was used for synthesis of ink.

4.2. Synthesis of 3D printable (Ag,Cu)₂(S,Se,Te)-based ink

The entire procedure was conducted under inert atmosphere (N_2) . TE powders with the stoichiometric composition of Ag_{0.1}Cu_{1.9}S_{0.25}-Se_{0.25}Te_{0.5} were prepared by mechanical alloying using a high-energy ball milling process (Fritsch Monomill, Pulverisette, Germany) under 450 rpm for 8 h. A zirconia (ZrO₂) milling jar with a volume of 80 ml was used with zirconia grinding balls ($\varphi = 5$ mm) and the weight ratio of balls to powder was 5:1. Te powders, serving as viscosifier and sintering agent, were produced through high-energy ball-milling (8000 M Mixer/ Mill, SPEX) within a 30-minute duration. The process involved stainless steel balls, comprising two balls ($\varphi=12.7$ mm) and four balls ($\varphi=12.7$ mm) 6.35 mm). Agglomerated particles were eliminated in all powders by sieving the particles to a size of $< 38 \mu m$. Combining 4 g of TE powder with the required Te additives, the mixture was dispersed in 3 g of glycerol. Subsequently, a planetary centrifugal mixer (ARM-100, Thinky) was employed for 30 minutes to ensure full homogenization of the ink.

4.3. Rheological properties of (Ag,Cu)₂(S,Se,Te)-based TE ink

The rheological properties of the $(Ag,Cu)_2(S,Se,Te)$ -based TE ink were investigated at room temperature using a oscillatory rheometer (Haake MARS III, Thermo Scientific) equipped with a coaxial cylinder geometry. During frequency sweep tests, a constant stress of 1 Pa was maintained, while stress sweep tests were carried out at frequencies of 1 rad/s with stress values ranging from 0.005 to 300 Pa. To examine the impact of Te additives on the viscoelastic properties of the TE inks, the rheological behaviors of $(Ag,Cu)_2(S,Se,Te)100/Tex$ (x=0,5,10,20) were evaluated.

4.4. 3D printing and sintering process of TE auxetic metamaterials

Three-dimensional printing was conducted using a self-built air-extrusion-based 3D printer with programmable pressure control. The TE ink was loaded into a 5 ml syringe barrel (Saejong) and a metal nozzle with an inner diameter of 360 μm was used. Using design software, the auxetic TE metamaterial was printed on a graphite substrate at room temperature (Video S1). The printed metamaterial was dried at 400 K for 24 h, and subsequently sintered with a two-step heat treatment process at 1003 K for 3 h, and 1123 K for 3–48 h in a box furnace under N_2 conditions.

4.5. Material characterization

XRD patterns were obtained using X'pert Pro (PANalytical) with a Cu $K\alpha$ X-ray source (wavelength, 1.5418 nm), operating at 40 kV and 30 mA, and equipped with an X'Celerator detector. The reference peaks of Cu₂Te corresponded to PDF #65-3460. Microstructure analysis was conducted using a field-effect SEM (FEI Nova NanoSEM 230 and S-4800 (Hitachi High-Tech)) at an operating voltage of 10 kV. OM images were captured using an Olympus BX51M instrument. The ζ potential of the particles was measured with a Zetasizer Nano ZS instrument (Malvern). Compression and bending tests were carried out at room temperature under uniaxial loading with a strain rate of 1×10^{-3} s⁻¹ using an Instron-5948 with a 2 kN load cell. Vibration tests were performed at room temperature using permanent electromagnet shaker (ET-139, Labworks Inc.) that was controlled using a function generator (AFG-2012, GW Instek) and a linear power amplifier (PA-138, Labworks Inc). The acceleration rate and displacement of the shaker at a frequency of 25 Hz was 10 g and 8 mm, respectively.

4.6. TE properties of 3D-printed samples

The temperature-dependent electrical conductivity and Seebeck coefficient were analyzed using a commercial instrument (SBA 458 Nemesis, NETZSCH) within the temperature range of 300-950 K under an argon (Ar) atmosphere. The thermal conductivity (κ) was determined using the formula $\kappa = \rho C_p D$, where ρ is density, C_p is specific heat capacity, and D is thermal diffusivity. The thermal diffusivity was measured using a laser flash analyser (LFA-457, NETZSCH) across the temperature range of 300-950 K. By measuring both the volume and weight of the cuboid shape, density was estimated, and the specific heat capacity was calculated using the Dulong-Petit equation. We evaluated the carrier concentrations and mobility using an equipment of HCS-1, LINSEIS, capable of generating dual opposing magnetic fields of ± 0.7 T. Thus, the measurement with this equipment provides three sets of data point which can plot the Hall voltage vs magnetic field (encompassing +0.7 T, 0 T, -0.7 T configurations). From the plot, we derived the Hall coefficient, carrier concentration, and mobility.

4.7. Fabrication and output power characterization of the auxetic TEGs

As the electrode, an Ag-containing adhesive (Pyro-Duct 597-A, Aremco) was used. To measure the temperature difference across the auxetic TEG, two K-type thermocouples were attached to the Ag electrode (hot side) and the upper surface of the auxetic TEG (cold side). To assess the power output characteristics of the auxetic TEG, we constructed a measurement setup in which the ceramic heater (25 mm \times 25 mm) consistently heated the underside of the alumina, while an air fan provided cooling to the cold side. To ensure accurate power generation measurement, the auxetic TEG was linked to a Keithley 2400 source-meter to record current–voltage (I–V) curves and the output power density for each temperature difference. The Keithley 2000 multimeter, connected to K-type thermocouples, was employed for the measurement of temperature differences. The maximum power output (P) was calculated using P = V² / 4 R, where V is the voltage and

R is the resistance.

4.8. Design of the auxetic metamaterials

The metamaterials were configured to fit the same printing platform, while having an identical volume, with uniform thickness (t) and width (w). To guide the design, the finite element analyses are used to understand mechanical behaviors of the metamaterials during the induced curvature change. Specifically, two types of simulations are employed: (1) three-dimensional solid analysis to account curvature change during the attachment to the curved heat source; (2) two-dimensional continuum analysis to model characteristic deformations of metamaterials of concern. Throughout the study, a linear elastic constitutive model with isotropic properties, namely Young's modulus of 9.608 GPa and Poisson's ratio of 0.35, derived from three-point bending tests on the (Ag, $\text{Cu}_{12}(\text{S},\text{Se},\text{Te})$ alloy is employed. Furthermore, geometric nonlinearity was considered to account for the deformation mechanisms of metamaterials incorporating non-negligible rigid-body displacement. Proprietary finite element software ABAQUS is used for all simulations.

In the three-dimensional simulation, the printed metamaterial was modelled by solids, and linear brick elements with hourglass control (C3D8R) was used accordingly. The upper and lower conformal surface were modelled as rigid bodies with the metamodel in between. To model the full attachment of the metamaterial to the heat source (i.e., lower surface) and observe the mechanical properties induced by such deformation, the lower surface is fixated while the upper surface was gradually displaced while ensuring quasi-static condition until the gap between the upper and lower surfaces corresponded to the thickness of metamaterials (Fig. S22). General contact settings, including hard contact for normal behavior and a tangential friction coefficient of 0.3, were implemented to control lateral movement of metamaterials and prevent surface penetration. Automatic stabilization was applied to effectively address nonlinear instability issues, with the maximum stabilization-tostrain energy ratio set at 0.005 and the dissipated energy fraction at 0.0002

For the two-dimensional analysis, Timoshenko elements with two nodes per element (B21) were utilized. The models assumed an ideal configuration of metamaterials, wherein one-dimensional beam elements were connected by hinges with zero bending rigidity, indicating that changes in strut angles do not induce stress, unlike changes in length. Despite this simplification, which limits detailed stress field within, the network model can capture the difference in deformation mechanisms between the metamaterials when their representative unit cells are subjected to isotropic eigenstrain (i.e., $\epsilon xx = \epsilon yy$). In the parametric analysis, the ranges of the three parameters were set as follows: $H \in [3,7]$, $L \in [1,5]$, and $\theta = [62]$. The unit cell's thickness (t) and width (w) were consistently set to 0.38 mm and 0.35 mm, respectively, throughout the study. The selected ranges for horizontal and inclined wall lengths (H and L) ensured at least two repetitions of the unit cell in each direction within the 3D printing platform, which is necessary for the coordinated behavior between unit cells. The θ range was determined based on the printing resolution.

4.9. Simulation of the TEG performance

We developed a three-dimensional finite element method (FEM) to calculate the temperature distribution in an auxetic TEG and resulting electrical outputs using commercial software COMSOL Multiphysics. The simulation was modeled using a heat transfer in solids module, electric currents module, multiphysics of the thermoelectric effect, and an electromagnetic heating model. A stationary study was conducted with a fully coupled solver. The design of TE leg was set to the auxetic structure composed of re-entrant unit cell with the optimized configuration. The TE leg was in contact with a curved alumina substrate with a curvature of 1/40 using Ag paste. The Ag paste layer was applied with a thickness of 0.1 mm, and its properties were defined as follows: an

electrical conductivity of $5 \times 10^5~S~m^{-1}$, a Seebeck coefficient of $0~V~K^{-1}$, a thermal conductivity of $9.1~W~m^{-1}~K^{-1}$, and a specific heat capacity (Cp) of $167~J~kg^{-1}~K^{-1}$. For the alumina substrate, the properties were specified as: an electrical conductivity of $1 \times 10^{-9}~S~m^{-1}$, a Seebeck coefficient of $0~V~K^{-1}$, a thermal conductivity of $20~W~m^{-1}~K^{-1}$, and a specific heat capacity of $800~J~kg^{-1}~K^{-1}$. The temperature-dependent thermoelectric properties of the 3D printed (Ag,Cu)₂(S,Se,Te) were applied to the designed TE leg, based on experimentally measured values as shown in Fig. 4. The boundary conditions were set to the fixed heat flow of the hot side at the bottom of the alumina substrate while applying forced convection to the other surface. The convection coefficient was set to $500~W~m^{-2}~K^{-1}$, and the ambient temperature was maintained at 300~K consistent with the experimental conditions. The contact resistance between the Ag paste and TE leg was applied to this TEG model based on the experiment.

The electrical potential of the open circuit (V_{oc}) was determined by applying an electrical ground to the bottom of Ag paste layer under open circuit conditions. The current of the short circuit (I_{sc}) was measured by applying the zero voltage to the top of TE layer to calculate the electrical resistance using the equation ($R = V_{oc}/I_{sc}$). The P was subsequently calculated using the equation ($P = V_{oc}^2/I_{sc}$). The system efficiency was calculated by dividing the P by the heat injected from the hot side (Q_h). For a comparative simulation study, a planar TE leg (11.4 mm \times 11.4 mm \times 0.35 mm) was used, which had the same material volume as the auxetic TE leg.

CRediT authorship contribution statement

Sangjoon Ahn: Methodology. Ju-Young Kim: Writing – original draft, Methodology. Hayoung Chung: Writing – original draft, Software, Methodology, Investigation, Data curation. Jae Sung Son: Writing – original draft, Visualization, Supervision, Project administration, Methodology, Data curation. So-Hyeon Lee: Methodology. Seungheon Shin: Software, Methodology. Jungsoo Lee: Visualization, Software. Youngtaek Oh: Writing – original draft, Validation, Software, Conceptualization. Seong Eun Yang: Writing – original draft, Validation, Methodology, Investigation, Formal analysis, Data curation, Conceptualization. Keonkuk Kim: Methodology. Changhyeon Nam: Methodology.

Declaration of Competing Interest

The authors declare the following financial interests/personal relationships which may be considered as potential competing interests: Jae Sung Son and Seong Eun Yang has patent META-STRUCTURE FLEXIBLE THERMOELECTRIC ELEMENT STRUCTURE AND MANUFACTURING METHOD pending to Pohang University of Science and Technology. If there are other authors, they declare that they have no known competing financial interests or personal relationships that could have appeared to influence the work reported in this paper.

Acknowledgements

This work was supported by the National Research Foundation of Korea (NRF) grant funded by the Ministry of Science and ICT (NRF-2020M3D1A1110502; NRF-2022R1A2C3009129; NRF-2021M3C1C 3097541; NRF-2020R1C1C1005741).

Appendix A. Supporting information

Supplementary data associated with this article can be found in the online version at doi:10.1016/j.nanoen.2024.110392.

Data availability

Data will be made available on request.

References

- P.E. Brockway, A. Owen, L.I. Brand-Correa, L. Hardt, Estimation of global finalstage energy-return-on-investment for fossil fuels with comparison to renewable energy sources, Nat. Energy 4 (2019) 612, https://doi.org/10.1038/s41560-019-0425-z.
- [2] S. Chu, A. Majumdar, Opportunities and challenges for a sustainable energy future, Nature 488 (2012) 294–303, https://doi.org/10.1038/nature11475.
- [3] L.E. Bell, Cooling, heating, generating power, and recovering waste heat with thermoelectric systems, Science 321 (2008) 1457–1461, https://doi.org/10.1126/ science 1158899
- [4] Q. Zhang, K. Deng, L. Wilkens, H. Reith, K. Nielsch, Micro-thermoelectric devices, Nat. Electron. 5 (2022) 333, https://doi.org/10.1038/s41928-022-00776-0.
- [5] S.I. Kim, K.H. Lee, H.A. Mun, H.S. Kim, S.W. Hwang, J.W. Roh, D.J. Yang, W. H. Shin, X.S. Li, Y.H. Lee, G.J. Snyder, S.W. Kim, Dense dislocation arrays embedded in grain boundaries for high-performance bulk thermoelectrics, Science 348 (2015) 109–114, https://doi.org/10.1126/science.aaa4166.
- [6] H. Hu, Y. Ju, J. Yu, Z. Wang, J. Pei, H.-C. Thong, J. Li, B. Cai, F. Liu, Z. Han, B. Su, H. Zhuang, Y. Jiang, H. Li, Q. Li, H. Zhao, B. Zhang, J. Zhu, J. Li, Highly stabilized and efficient thermoelectric copper selenide, Nat. Mater. 23 (2024) 527–534, https://doi.org/10.1038/s41563-024-01815-1.
- [7] B. Jiang, Y. Yu, J. Cui, X. Liu, L. Xie, J. Liao, Q. Zhang, Y. Huang, S. Ning, B. Jia, B. Zhu, S. Bai, L. Chen, S.J. Pennycook, J. He, High-entropy-stabilized chalcogenides with high thermoelectric performance, Science 371 (2021) 830–834, https://doi.org/10.1126/science.abe1292.
- [8] M. Pettigrew, Y. Sylvestre, A. Campagna, Vibration analysis of heat exchanger and steam generator designs, Nucl. Eng. Des. 48 (1978) 97–115, https://doi.org/ 10.1016/0029-5493(78)90211-X.
- [9] M.T. Pittard, R.P. Evans, R.D. Maynes, J.D. Blotter, Experimental and numerical investigation of turbulent flow induced pipe vibration in fully developed flow, Rev. Sci. Instrum. 75 (2004) 2393–2401, https://doi.org/10.1063/1.1763256.
- [10] F. Kim, B. Kwon, Y. Eom, J.E. Lee, S. Park, S. Jo, S.H. Park, B.S. Kim, H.J. Im, M. H. Lee, T.S. Min, K.T. Kim, H.G. Chae, W.P. King, J.S. Son, 3D printing of shape-conformable thermoelectric materials using all-inorganic Bi₂Te₃-based inks, Nat. Energy 3 (2018) 301–309, https://doi.org/10.1038/s41560-017-0071-2.
- [11] D. Bao, J. Chen, Y. Yu, W. Liu, L. Huang, G. Han, J. Tang, D. Zhou, L. Yang, Z.-G. Chen, Texture-dependent thermoelectric properties of nano-structured Bi₂Te₃, Chem. Eng. J. 388 (2020) 124295, https://doi.org/10.1016/j.cej.2020.124295.
- [12] Y. Gelbstein, G. Gotesman, Y. Lishzinker, Z. Dashevsky, M. Dariel, Mechanical properties of PbTe-based thermoelectric semiconductors, Scr. Mater. 58 (2008) 251–254, https://doi.org/10.1016/j.scriptamat.2007.10.012.
 [13] X. Liu, Y. Chen, H. Wang, S. Liu, B. Zhang, X. Lu, G. Wang, G. Han, X. Chen,
- [13] X. Liu, Y. Chen, H. Wang, S. Liu, B. Zhang, X. Lu, G. Wang, G. Han, X. Chen, X. Zhou, Simultaneously enhanced thermoelectric and mechanical performance in SnSe-based nanocomposites produced via sintering SnSe and KCuyS₄ nanomaterials, ACS Appl. Mater. Interfaces (2024), https://doi.org/10.1021/ acsami 3c14754
- [14] K. Bertoldi, V. Vitelli, J. Christensen, M. Van Hecke, Flexible mechanical metamaterials, Nat. Rev. Mater. 2 (2017) 1–11, https://doi.org/10.1038/ paterymats 2017.66
- [15] J.U. Surjadi, L. Gao, H. Du, X. Li, X. Xiong, N.X. Fang, Y. Lu, Mechanical metamaterials and their engineering applications, Adv. Eng. Mater. 21 (2019) 1800864, https://doi.org/10.1002/adem.201800864.
- [16] H.M. Kolken, A. Zadpoor, Auxetic mechanical metamaterials, RSC Adv. 7 (2017) 5111–5129, https://doi.org/10.1039/C6RA27333E.
- [17] M. Mir, M.N. Ali, J. Sami, U. Ansari, Review of mechanics and applications of auxetic structures, Adv. Mater. Sci. Eng. 2014 (2014) 753496, https://doi.org/ 10.1155/2014/753496.
- [18] T. Li, F. Liu, L. Wang, Enhancing indentation and impact resistance in auxetic composite materials, Compos. B Eng. 198 (2020) 108229, https://doi.org/ 10.1016/j.compositesb.2020.108229.
- [19] R.S. Naboni, L. Mirante, in SIGRADI 2015: Informação de projeto para interação. (Blucher Design Proceedings, (2015), pp. 129-136, https://dx.doi.org/10.5151/desprosignadi2015-30268
- [20] J. Rasburn, P.G. Mullarkey, K.E. Evans, A. Alderson, S. Ameer-Beg, W. Perrie, Auxetic structures for variable permeability systems, AICHE J. 47 (2001) 2623–2626, https://doi.org/10.1002/aic.690471125.
- [21] M. Najafi, H. Ahmadi, G. Liaghat, Experimental investigation on energy absorption of auxetic structures, Mater. Today. Proc. 34 (2021) 350–355, https://doi.org/ 10.1016/j.matpr.2020.06.075.
- [22] X. Shi, H. Chen, F. Hao, R. Liu, T. Wang, P. Qiu, U. Burkhardt, Y. Grin, L. Chen, Room-temperature ductile inorganic semiconductor, Nat. Mater. 17 (2018) 421–426, https://doi.org/10.1038/s41563-018-0047-z.
- [23] Q. Yang, S. Yang, P. Qiu, L. Peng, T.-R. Wei, Z. Zhang, X. Shi, L. Chen, Flexible thermoelectrics based on ductile semiconductors, Science 377 (2022) 854–858, https://doi.org/10.1126/science.abq0682.
- [24] S. He, Y. Li, L. Liu, Y. Jiang, J. Feng, W. Zhu, J. Zhang, Z. Dong, Y. Deng, J. Luo, W. Zhang, G. Chen, Semiconductor glass with superior flexibility and high room temperature thermoelectric performance, Sci. Adv. 6 (2020) eaaz8423, https://doi. ore/10.1126/sciadv.aaz8423.
- [25] Z. Gao, Q. Yang, P. Qiu, T.-R. Wei, S. Yang, J. Xiao, L. Chen, X. Shi, P-type plastic inorganic thermoelectric materials, Adv. Energy Mater. 11 (2021) 2100883, https://doi.org/10.1002/aenm.202100883.
- [26] X. Liang, C. Chen, Ductile inorganic amorphous/crystalline composite Ag₄Te_S with phonon-glass electron-crystal transport behavior and excellent stability of high thermoelectric performance on plastic deformation, Acta Mater. 218 (2021) 117231, https://doi.org/10.1016/j.actamat.2021.117231.

- [27] Z. Zhang, K. Zhao, H. Chen, Q. Ren, Z. Yue, T.-R. Wei, P. Qiu, L. Chen, X. Shi, Entropy engineering induced exceptional thermoelectric and mechanical performances in Cu_{2.y}AgyTe_{1.2x}S_xSe_x, Acta Mater. 224 (2022) 117512, https://doi. org/10.1016/j.actamat.2021.117512
- [28] H. Chen, C. Shao, S. Huang, Z. Gao, H. Huang, Z. Pan, K. Zhao, P. Qiu, T.-R. Wei, X. Shi, High-entropy cubic pseudo-ternary Ag₂(S, Se, Te) materials with excellent ductility and thermoelectric performance, Adv. Energy Mater. 14 (2023) 2303473, https://doi.org/10.1002/aenm.202303473.
- [29] R. v Mises, Mechanik der festen Körper im plastisch-deformablen Zustand, Nachr. Ges. Wiss. Goettingen, Math. Phys. Kl. 1913 (1913) 582–592.
- [30] J. Huang, Q. Zhang, F. Scarpa, Y. Liu, J. Leng, Multi-stiffness topology optimization of zero Poisson's ratio cellular structures, Compos. B Eng. 140 (2018) 35–43, https://doi.org/10.1016/j.compositesb.2017.12.014.
- [31] M. Zeng, D. Zavanelli, J. Chen, M. Saeidi-Javash, Y. Du, S. Leblanc, G.J. Snyder, Y. Zhang, Printing thermoelectric inks toward next-generation energy and thermal devices, Chem. Soc. Rev. 51 (2022) 485, https://doi.org/10.1039/D1CS00490E.
- [32] S.H. Park, S. Jo, B. Kwon, F. Kim, H.W. Ban, J.E. Lee, D.H. Gu, S.H. Lee, Y. Hwang, J.-S. Kim, D.-B. Hyun, S. Lee, K.J. Choi, W. Jo, J.S. Son, High-performance shape-engineerable thermoelectric painting, Nat. Commun. 7 (2016) 13403, https://doi.org/10.1038/ncomms13403.
- [33] S.E. Yang, F. Kim, F. Ejaz, G.S. Lee, H. Ju, S. Choo, J. Lee, G. Kim, S.-H. Jung, S. Ahn, H.G. Chae, K.T. Kim, B. Kwon, J.S. Son, Composition-segmented BiSbTe thermoelectric generator fabricated by multimaterial 3D printing, Nano Energy 81 (2021) 105638, https://doi.org/10.1016/j.nanoen.2020.105638.
- [34] S. Choo, F. Ejaz, H. Ju, F. Kim, J. Lee, S.E. Yang, G. Kim, H. Kim, S. Jo, S. Baek, Cu₂Se-based thermoelectric cellular architectures for efficient and durable power generation, Nat. Commun. 12 (2021) 3550, https://doi.org/10.1038/s41467-021-23044 pt
- [35] J. Lee, S. Choo, H. Ju, J. Hong, S.E. Yang, F. Kim, D.H. Gu, J. Jang, G. Kim, S. Ahn, J.E. Lee, S.Y. Kim, H.G. Chae, J.S. Son, Doping-induced viscoelasticity in PbTe thermoelectric inks for 3D printing of power-generating tubes, Adv. Energy Mater. 11 (2021) 2100190, https://doi.org/10.1002/aenm.202100190.
- [36] S. Griffin, M. Sarfraz, S.F. Hartmann, S.R. Pinnapireddy, M.J. Nasim, U. Bakowsky, C.M. Keck, C. Jacob, Resuspendable powders of lyophilized chalcogen particles with activity against microorganisms, Antioxidants 7 (2018) 23, https://doi.org/ 10.3390/antiox7020023.
- [37] G. Guisbiers, L.C. Mimun, R. Mendoza-Cruz, K.L. Nash, Synthesis of tunable tellurium nanoparticles, Semicond. Sci. Technol. 32 (2017) 04LT01, https://doi. org/10.1088/1361-6641/aa6173.
- [38] G. Guisbiers, Q. Wang, E. Khachatryan, L.C. Mimun, R. Mendoza-Cruz, P. Larese-Casanova, T.J. Webster, K.L. Nash, Inhibition of E. coli and S. aureus with selenium nanoparticles synthesized by pulsed laser ablation in deionized water, Int. J. Janomed. 11 (2016), https://doi.org/10.2147/JJN.S106289.
- [39] Z. Wang, X. Dong, X.-F. Li, Y. Feng, S. Li, W. Tang, Z.L. Wang, A contact-electrocatalysis process for producing reactive oxygen species by ball milling of triboelectric materials, Nat. Commun. 15 (2024) 757, https://doi.org/10.1038/ s41467-024-45041-4.
- [40] M.U. Ghori, E. Šupuk, B.R. Conway, Tribo-electrification and powder adhesion studies in the development of polymeric hydrophilic drug matrices, Materials 8 (2015) 1482–1498, https://doi.org/10.3390/ma8041482.
- [41] D. Zhang, X.J.G. Lim, X. Li, K. Saglik, S.F.D. Solco, X.Y. Tan, Y. Leow, W. Zhai, C.K. I. Tan, J. Xu, A. Suwardi, 3D-printed porous thermoelectrics for in situ energy harvesting, ACS Energy Lett. 8 (2022) 332–338, https://doi.org/10.1021/acsenersylett.202425.
- [42] W.D. Liu, L. Yang, Z.G. Chen, J. Zou, Promising and eco-friendly Cu2X-based thermoelectric materials: progress and applications, Adv. Mater. 32 (2020) 1905703, https://doi.org/10.1002/adma.201905703.
- 1905703, https://doi.org/10.1002/adma.201905703.
 [43] Y.F. Kao, S.K. Chen, T.J. Chen, P.C. Chu, J.W. Yeh, S.J. Lin, Electrical, magnetic, and hall properties of Al_xCoCrFeNi high-entropy alloys, J. Alloy. Compd. 509 (2011) 1607–1614, https://doi.org/10.1016/j.jallcom.2010.10.210.
- [44] S. Zhi, J. Li, L. Hu, J. Li, N. Li, H. Wu, F. Liu, C. Zhang, W. Ao, H. Xie, X. Zhao, S. J. Pennycook, T. Zhu, Medium entropy-enabled high performance cubic GeTe thermoelectrics, Adv. Sci. 8 (2021) 2100220, https://doi.org/10.1002/advs.202100220
- [45] Y. He, P. Lu, X. Shi, F. Xu, T. Zhang, G.J. Snyder, C. Uher, L. Chen, Ultrahigh thermoelectric performance in mosaic crystals, Adv. Mater. 27 (2015) 3639–3644, https://doi.org/10.1002/adma.201501030.
- [46] H.-S. Kim, Z.M. Gibbs, Y. Tang, H. Wang, G.J. Snyder, Characterization of Lorenz number with Seebeck coefficient measurement, APL Mater. 3 (2015), https://doi. org/10.1063/1.4908244
- [47] X. Chen, S. Wu, J. Zhou, Influence of porosity on compressive and tensile strength of cement mortar, Constr. Build. Mater. 40 (2013) 869–874, https://doi.org/ 10.1016/j.conbuildmat.2012.11.072.
- [48] J. Bu, Z. Tian, Relationship between pore structure and compressive strength of concrete: experiments and statistical modeling, Sādhanā 41 (2016) 337–344, https://doi.org/10.1007/s12046-016-0468-9.
- [49] J. Schroers, W.L. Johnson, Ductile bulk metallic glass, Phys. Rev. Lett. 93 (2004) 255506, https://doi.org/10.1103/PhysRevLett.93.255506.
- [50] K. Tyagi, B. Gahtori, S. Bathula, M. Jayasimhadri, S. Sharma, N.K. Singh, D. Haranath, A.K. Srivastava, A. Dhar, Crystal structure and mechanical properties of spark plasma sintered Cu₂Se: an efficient photovoltaic and thermoelectric material, Solid State Commun. 207 (2015) 21–25, https://doi.org/10.1016/j. ssc 2015 02 004
- [51] C. Lee, G. Song, M.C. Gao, R. Feng, P. Chen, J. Brechtl, Y. Chen, K. An, W. Guo, J. D. Poplawsky, S. Li, A.T. Samaei, W. Chen, A. Hu, H. Choo, P.K. Liaw, Lattice

- distortion in a strong and ductile refractory high-entropy alloy, Acta Mater. 160 (2018) 158–172, https://doi.org/10.1016/j.actamat.2018.08.053.
- [52] Y. Zheng, Q. Zhang, X. Su, H. Xie, S. Shu, T. Chen, G. Tan, Y. Yan, X. Tang, C. Uher, G.J. Snyder, Mechanically robust BiSbTe alloys with superior thermoelectric performance: a case study of stable hierarchical nanostructured thermoelectric materials, Adv. Energy Mater. 5 (2015) 1401391, https://doi.org/10.1002/aepm.201401391.
- [53] Y.J. Liu, X.D. Wang, S.H. Hou, Z.X. Wu, J. Wang, J. Mao, Q. Zhang, Z.G. Liu, F. Cao, Scalable-produced 3D elastic thermoelectric network for body heat harvesting, Nat. Commun. 14 (2023) 3058, https://doi.org/10.1038/s41467-023-38852-4.
- [54] S. Xu, M. Hong, X. Shi, M. Li, Q. Sun, Q. Chen, M. Dargusch, J. Zou, Z.-G. Chen, Computation-guided design of high-performance flexible thermoelectric modules for sunlight-to-electricity conversion, Energy Environ. Sci. 13 (2020) 3480–3488, https://doi.org/10.1039/D0EE01895C.
- [55] T. Sun, B. Zhou, Q. Zheng, L. Wang, W. Jiang, G.J. Snyder, Stretchable fabric generates electric power from woven thermoelectric fibers, Nat. Commun. 11 (2020) 572, https://doi.org/10.1038/s41467-020-14399-6.
- [56] Y. Han, L.E. Simonsen, M.H. Malakooti, Printing liquid metal elastomer composites for high-performance stretchable thermoelectric generators, Adv. Energy Mater. 12 (2022) 2201413, https://doi.org/10.1002/aenm.202201413.

- [57] S.J. Kim, J.H. We, B.J. Cho, A wearable thermoelectric generator fabricated on a glass fabric, Energy Environ. Sci. 7 (2014) 1959–1965, https://doi.org/10.1039/ C4FF00242C
- [58] B. Lee, H. Cho, K.T. Park, J.S. Kim, M. Park, H. Kim, Y. Hong, S. Chung, High-performance compliant thermoelectric generators with magnetically self-assembled soft heat conductors for self-powered wearable electronics, Nat. Commun. 11 (2020) 5948, https://doi.org/10.1038/s41467-020-19756-z.
- [59] P. Zhu, C. Shi, Y. Wang, Y. Wang, Y. Yu, Y. Wang, Y. Deng, J. Xiao, Recyclable, healable, and stretchable high-power thermoelectric generator, Adv. Energy Mater. 11 (2021) 2100920, https://doi.org/10.1002/aenm.202100920.
- [60] Y. Yang, H. Hu, Z. Chen, Z. Wang, L. Jiang, G. Lu, X. Li, R. Chen, J. Jin, H. Kang, H. Chen, S. Lin, S. Xiao, H. Zhao, R. Xiong, J. Shi, Q. Zhou, S. Xu, Y. Chen, Stretchable nanolayered thermoelectric energy harvester on complex and dynamic surfaces, Nano Lett. 20 (2020) 4445–4453, https://doi.org/10.1021/acs.
- [61] H. Choi, B.-K. Min, S.-J. Joo, B.-S. Kim, K. Lee, H. Kang, Y.H. Sim, M.J. Yun, D. Y. Lee, S.I. Cha, Partially air-filled skin-attachable deformable gasket with negative poisson's ratio for highly-efficient stretchable thermoelectric generators, Adv. Energy Mater. 13 (2023) 2301252, https://doi.org/10.1002/aenm.202301252.